Journal of Materials Chemistry A

Facile and scalable dry surface doping technique to enhance the electrochemical performance of LiNi0.64Mn0.2Co0.16O2 cathode materials

Journal:	*Journal of Materials Chemistry A*
Manuscript ID	TA-ART-08-2020-007779.R1
Article Type:	Paper
Date Submitted by the Author:	11-Sep-2020
Complete List of Authors:	Shi, Yang; A123 Systems LLC, Kim, Kitae; A123 Systems LLC Xing, Yingjie; A123 Systems LLC Millonig, Andrew; A123 Systems LLC Kim, Bryan; A123 Systems LLC Wang, Lixin; A123 Systems LLC Lee, Eunsung; A123 Systems LLC Harrison, Chloe; A123 Systems LLC Yu, Taehwan; A123 Systems LLC Johnson, Derek; A123 Systems LLC Lipson, Albert; Argonne National Lab, Durham, Jessica; Argonne National Laboratory Liu, Donghao; Argonne National Laboratory Fister, Timothy; Argonne National Laboratory Yu, Lei; Argonne National Laboratory Wen, Jianguo; Argonne National Laboratory

ARTICLE

Facile and scalable dry surface doping technique to enhance the electrochemical performance of $LiNi_{0.64}Mn_{0.2}Co_{0.16}O_2$ cathode materials

Received 00th January 20xx,
Accepted 00th January 20xx

DOI: 10.1039/x0xx00000x

Yang Shi,[a] Kitae Kim,[a] Yingjie Xing,[a] Andrew Millonig,[a] Bryan Kim,[a] Lixin Wang,[a] Eunsung Lee,[a] Chloe Harrison,[a] Taehwan Yu,[a] Derek C. Johnson,[a] Albert L. Lipson,[b] Jessica L. Durham,[b] Donghao Liu,[b] Timothy T. Fister,[c] Lei Yu,[d] and Jianguo Wen[d]

Lithium nickel manganese cobalt oxide (NMC) is one of the dominant cathode materials in lithium-ion batteries. Here a simple, efficient and scalable surface doping technique is successfully demonstrated, which can be readily used in mass production of cathode materials. For the first time neodymium oxide (Nd2O3) has been employed as the surface doping agent. The Nd-doped NMC shows greatly improved cycling and rate performance, and the enhanced cycling stability has been demonstrated in full pouch cells, with a 17.5% increase in capacity retention after 300 cycles. Fewer cracks have been observed in the doped NMC after cycling, and in-situ X-ray diffraction reveals the suppressed lattice collapse by Nd doping. Greatly suppressed surface phase change has been confirmed by HR-TEM and EELS. The result suggests great promise in using this dry doping technique to enhance the electrochemical performance of NMC cathodes.

Introduction

Lithium-ion (Li^+) batteries are becoming the dominant power sources for portable electronics and electric vehicles, due to their high energy density (260 Wh kg^{-1} and 700 Wh L^{-1} at cell level).[1,2] Lithium nickel manganese cobalt oxide (NMC) with high Ni content (Ni>60%) is one of the most promising cathode materials due to its relatively high capacity and low cost. However, the fast capacity decay and resistance growth during cycling still limit its application. Great efforts have been made to address this issue, and doping NMC cathode material with metal ions can improve their electrochemical performance.[3-5] However, in bulk doping, which is achieved by either doping the hydroxide or carbonate precursors[6] or mixing a doping agent with the precursors and lithium source followed by sintering[7], specific capacity may be sacrificed due to the electrochemical inactivity of dopants in the core of the cathode particle. The surface of the NMC cathode material is exposed to electrolyte and therefore is more vulnerable to phase change and side reactions, which greatly contribute to capacity degradation.[8, 9] Therefore, restricting the doping to the cathode surface can be efficient in stabilizing the structure. This surface doping is readily achieved by directly reacting the cathode with the doping agent at temperatures that limit the diffusivity of the dopant ion into the core of NMC particles.

A wet doping process was developed to achieve surface doping, in which cathode materials were mixed with doping agents in ethanol, followed by evaporation of solvents and calcination.[10] However, the efficacy may be restricted by two issues. Firstly, the high cost of organic solvents results in higher costs during manufacturing. Secondly, the processing costs can increase due to the additional procedures necessary to remove the solvents, as well as waste management. If water is used as the solvent, it may affect the structure and the composition on the surface of the cathode material. Specifically, the leaching of Li^+ by water may lead to surface Li^+ deficiency, accompanied by phase change.

A dry surface doping process, in which no solvent is used, has advantages over wet surface doping since it eliminates the contact between the cathode materials and water or an organic solvent which may result in possible damage to the cathode surface. A dry doping process eliminates the multi-step drying process to remove the solvent and the necessity of waste management. Both metal oxides and metal salts have the potential to be employed as doping agents, where the former has advantages over the latter because metal oxides can possess well-tuned particle sizes during manufacturing, compared to metal salts. Dry surface doping requires a solid-state reaction between the cathode and doping agents, and such a reaction can be facilitated by utilizing small-size metal oxides.

[a] A123 Systems, LLC, 200 West Street, Waltham, MA 02451. E-mail: yshi@a123systems.com
[b] Applied Materials Division, Argonne National Laboratory, 9700 S Case Avenue, Lemont, IL 60439.
[c] Chemical Sciences and Engineering Division, Argonne National Laboratory, 9700 S Case Avenue, Lemont, IL 60439.
[d] Center for Nanoscale Materials, Argonne National Laboratory, 9700 S Case Avenue, Lemont, IL 60439.

†Electronic Supplementary Information (ESI) available: [XRD, TEM, EELS]. See DOI: 10.1039/x0xx00000x

Metal oxides with high stability against the NMC cathode have been investigated as coating materials, such as Al_2O_3, SiO_2, and ZrO_2.[11-14] However, to the best of our knowledge, metal oxides have not been investigated as surface doping agents. This might be due to the limitation in reaction temperature: the reaction temperature between NMC and metal oxides as doping agents should not exceed 900 °C, due to crystal growth and Li loss. Based on this selection criterion, we have screened various metal oxide candidates. Our screening was not limited to elements whose ionic radius are similar to Li^+ (0.90 Å), Ni^{2+} (0.83 Å), Ni^{3+}[LS] (0.74 Å), Co^{3+} [LS] (0.685 Å), and Mn^{4+}(0.67 Å).[15] Dopants with large ionic radius have a "pillar effect" to support the crystal structure during delithiation and lithiation processes, and larger dopants tend to expand the *c* lattice to enhance the rate capability. In considering of both these two factors, reaction temperature and ionic radius, we selected Nd_2O_3 as the doping agent. Nd_2O_3 can react with NMC at temperatures below 750 °C, and it has a large ionic radius (Nd^{3+}=0.098) which may serve as "pillars" to stabilize the crystal structure. The "pillar effect" may help suppress the lattice volume change, and therefore suppress the formation and growth of cracks. Cracking exposes more of the cathode surface area to the electrolyte, thus allowing for side reactions between the cathode and the electrolyte which leads to capacity degradation. In addition, large Nd^{3+} ions may expand the *c* lattice and enhance the rate capability.

In this work, for the first time Nd_2O_3 has been employed as the doping agent for dry surface doping. By mixing the Nd_2O_3 with NMC material, followed by a calcination step, the cycling performance and rate capability of the NMC material is significantly improved. Meanwhile the crack formation and growth in cathode materials during cycling is suppressed. The result suggests great promise in using this simple yet efficient dry doping process to improve the electrochemical performance of NMC cathode materials.

Experimental

Materials synthesis and Characterization

Nd_2O_3 particles (80-140 nm) and lithium nickel cobalt manganese ($LiNi_{0.64}Mn_{0.2}Co_{0.16}O_2$, NMC, from BASF) were mixed via ball milling in a roller mill to achieve uniform dispersion of the former on the surface of the latter. The molar ratios of Nd in NMC powder are 0.3%, 0.6% and 0.9%. The mixture was sintered in air at a temperature of 750 °C for 4 h with a ramping rate of 5 °C/min, followed by natural cooling to obtain the Nd-doped NMC powder. Pure NMC powder was also sintered in air at 750 °C for 4 h without Nd doping, as a reference sample. Thermogravimetric analysis (TGA, Netzsch Jupiter STA 499 C) was performed to determine the sintering temperature. The doped-NMC powder was characterized by scanning electron microscope (SEM, Amray 3300 FE-SEM) with Energy Dispersive X-Ray Spectroscopy (EDS) detector (SiriusSD 30 mm SDD). Cross-polishing of electrodes was carried out by a JEOL IB-19530CP cross-section polisher. The composition of pristine, annealed, and Nd-doped NMC cathode materials was measured by an ICP-OES (Leeman Lab). *Ex-situ* X-ray diffraction (XRD, Rigaku Miniflex 600) was performed to obtain the morphology and crystal structure of Nd-doped NMC.

Electrochemical characterization-half coin cells

Electrochemical characterization of the doped NMC powder was first evaluated in coin cells with a metallic Li anode. To prepare the cathode electrode for coin cell testing, 93 wt.% pristine or doped NMC powder, 4 wt.% carbon conductive additives (Denka), 3 wt.% polyvinylidene fluoride (PVDF) binder (5% HSV-900 PVDF in N-Methyl-2-pyrrolidone solution) were mixed in a Thinky mixer for 5 min at 2000 RPM for three times. The resulting slurry was cast on aluminum foil with a doctor blade and the active mass loading was controlled at 7 mg/cm^2. After drying the cast electrode in a vacuum oven at 85 °C for 12 h, it was calendered to an electrode density of 3.3 g/cm^3 to form the final cathode electrode with a diameter of 15 mm. Type-2025 coin cells were assembled with the cathode electrode, a lithium disk as the anode, and Celgard 2500 membrane as the separator. The electrolyte was 1M $LiPF_6$ in a mixture of ethylene carbonate (EC) and ethyl methyl carbonate (EMC) solvents (v:v=1:2). The assembled coin cells were tested in the voltage range of 2.7-4.3 V.

Electrochemical characterization-pouch full cells

The Nd-doped NMC powder was further evaluated in single layer pouch cells. The cathode electrode was composed of 94.5 wt.% pristine or doped NMC powder, 2.5 wt.% carbon conductive additives (2% wt. Denka Black and 0.5% wt. ECP), and 3 wt.% PVDF (Solvay 5130). The anode electrode was composed of 94.5 wt.% graphite, 1 wt.% vapor grown carbon fibers (VGCF), 1.5 wt.% carboxymethyl cellulose (CMC) and 0.5 wt.% styrene-butadiene rubber (SBR). The active mass loading was 18.40 g/cm^2 for the cathode and 11 g/cm^2 for the anode. The same separator and electrolyte were used in the assembly of full cells. The single layer pouch cells were tested in the voltage range of 2.75-4.2 V.

In-situ XRD: X-ray diffraction was measured at sector 13BM-C at the Advanced Photon Source at Argonne National Laboratory using a side-deflecting Rowland circle Si (311) monochromator, which provided a 28.7 keV source (0.433 Å) focused to 300 × 200 μm^2. Powder diffraction was measured by twenty second exposures on a Pilatus 1M detector 200 mm downstream from the sample. Calibration was taken using a LaB_6 standard at the sample position. Using this calibrant, integration and background subtraction of the raw data were completed by Dioptas[16] while sequential refinements were performed using GSAS-II.[17] Multiple cells were cycled at C/10 using x-ray-compatible 2032 coin cells. Each cell had a 3 mm aperture on the outer housing that was internally sealed with a fluorosilicone gasket. Glassy carbon disks, which are nearly x-ray transparent at this energy, replaced the stainless steel spacers within the cell, providing both stack pressure and conductivity to the cathode laminate and lithium anode. External polyimide windows were also used as a secondary seal.

Microscopic characterization

High resolution transmission electron microscopy (HRTEM) was taken using a JEOL JEM-2100F at 200 kV accelerating voltage in TEM mode. Electron energy loss spectroscopy (EELS) samples were prepared by first coating with gold and then ion beam deposited platinum or carbon. The samples were attached to the TEM grid and polished to about 100 nm thickness using a focused ion beam (Zeiss Nvision 40). EELS spectroscopy was done at 200 kV accelerating voltage in a FEI Tecnai F20ST using a Gatan EELS system. Background subtraction using a power law fit in the pre-edge region was performed in FEI TIA software and a 5 point Savitzky-Golay smoothing algorithm was used to reduce noise. Energy dispersion was corrected by using a cubic fit to the O, Mn, Co and Ni edge peaks in the bulk materials to 544 eV, 644.5 eV, 782 eV and 854 eV respectively.

Results and Discussion

To determine the appropriate sintering temperature for the doping reaction, TGA was performed for pure NMC powder and the mixture of NMC and Nd_2O_3 particles. A higher than normal dosage of Nd_2O_3 in NMC powder (33 wt. %) was selected in order to clearly observe the change in weight. Fig. 1 shows the weight change of samples as a function of temperature. In the case of pure NMC, the slight weight loss is due to the slight oxygen release at temperatures higher than 500 °C. When the temperature is higher than 900 °C, the oxygen loss is more severe. In the case of the mixture of NMC and Nd_2O_3 powder, obvious weight loss in the temperature range of 676.2-711.8 °C is observed, indicating the reaction of NMC with Nd_2O_3, accompanied by the release of oxygen. Therefore, 750 °C has been selected as the sintering temperature for the doping reaction.

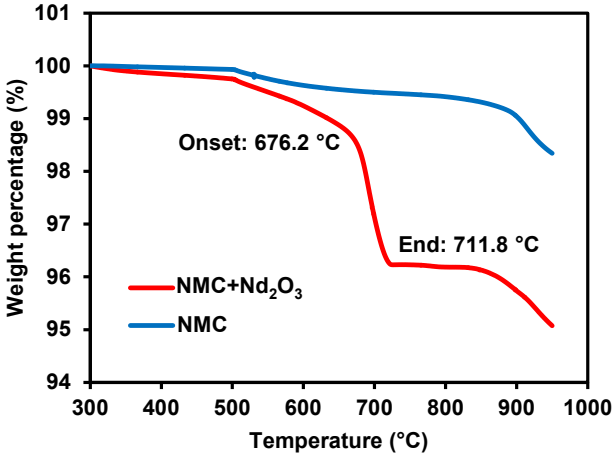

Fig. 1 TGA plot of pure NMC and the mixture of NMC and Nd_2O_3.

Fig. 2a shows the morphology of the mixture of Nd_2O_3 and NMC powder before sintering, with the small particles in the range of 80-140 nm being Nd_2O_3 nanoparticles. After sintering (**Fig. 2b-c**), the Nd_2O_3 can no longer be observed, indicating that Nd_2O_3 has reacted with the NMC powder and Nd has been doped into NMC. The SEM-EDS mapping of Nd in doped NMC shows well distributed Nd (Fig. 2d). The TEM-EDS mapping of the cross-section of the Nd-doped NMC shows that Nd is distributed on the surface (Fig. S1). Table 1 shows the compositions of the materials measured by ICP-OES, as well as the lattice parameters from the XRD measurement, by Rietveld refinement using the structural model. The XRD patterns with refinement are displayed in Fig. S2. The pristine, annealed and Nd-doped NMC samples show similar lattice parameters, indicating Nd surface doping does not change the bulk crystal structure of the NMC cathode.

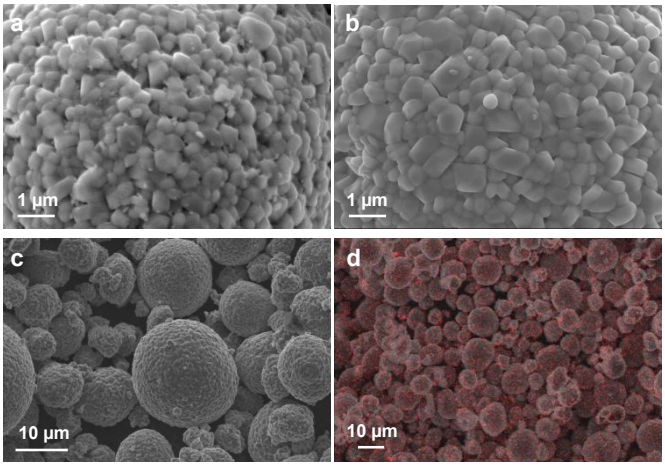

Fig. 2 SEM images of (a) the mixture of Nd_2O_3 and NMC powder before sintering, (b) Nd-doped NMC (after sintering)-high magnification, (c) Nd-doped NMC-low magnification, and (d) Nd EDS mapping of Nd-doped NMC.

Table 1 Compositions and lattice parameters of pristine, annealed and Nd-doped NMC.

	Composition	*a*	*c*	I_{003}/I_{104}
NMC	$Li_{1.025}Ni_{0.644}Co_{0.159}Mn_{0.197}O_2$	2.865(3)	14.196(2)	1.431
Annealed NMC	$Li_{1.023}Ni_{0.645}Co_{0.161}Mn_{0.194}O_2$	2.864(9)	14.197(5)	1.429
Nd-doped NMC	$Li_{1.020}Nd_{0.006}Ni_{0.641}Co_{0.162}Mn_{0.197}O_2$	2.864(6)	14.202(1)	1.497

NMC cathodes doped with different amount of Nd (0.3%, 0.6%, and 0.9%) were first tested in coin cells and the 0.6% Nd-doped sample showed the best cycling performance (Fig. S3). Therefore, the rest of the testing was performed on the 0.6% Nd-doped sample, denoted as Nd-doped NMC. As Fig. 3a shows, the pristine NMC shows a discharge capacity of 183.7 mAh/g in the first cycle at C/10. Without doping, annealed NMC shows slightly increased capacity of 184.7 mAh/g. The Nd-doped NMC shows decreased capacity (181.6 mAh/g) compared to the pristine NMC. In terms of the rate performance at C/5, C/2, 1C, 2C, 5C (Fig. 3b), the pristine NMC shows discharge capacities of 175.9, 170.4, 165.5, 160.1, and 149.5 mAh/g, respectively; the annealed NMC shows slightly

increased discharge capacities of 176.9, 171.5, 166.5, 161, 151 mAh/g, respectively; the Nd-doped NMC shows increased discharge capacities of 178.4, 173.4, 168.8, 163.5, and 154.7 mAh/g, respectively. The Nd-doped NMC shows slightly lower capacity at low rate (C/10), which is due to the electrochemical inactivity of Nd. However, it shows higher capacities at high rate (C/2-5C), which is due to the large ionic radius of Nd that can expand the *c* lattice on the surface of NMC after doping and help facilitate the transport of Li^+ on the surface. The increased specific capacity of the annealed NMC is probably due to the reduced NiO phase or relaxation of stress/strain after heat treatment.[18, 19] In addition to the improved rate capability, the Nd-doped NMC also shows better cycling performance than the pristine NMC (Fig. 3c). The Nd-doped NMC still maintains a discharge capacity of 162.2 mAh/g after 100 cycles, while the pristine NMC only shows 153.4 mAh/g after 100 cycles. The annealed-only NMC shows slightly increased specific capacity, while its cycling performance is still worse than the Nd-doped NMC.

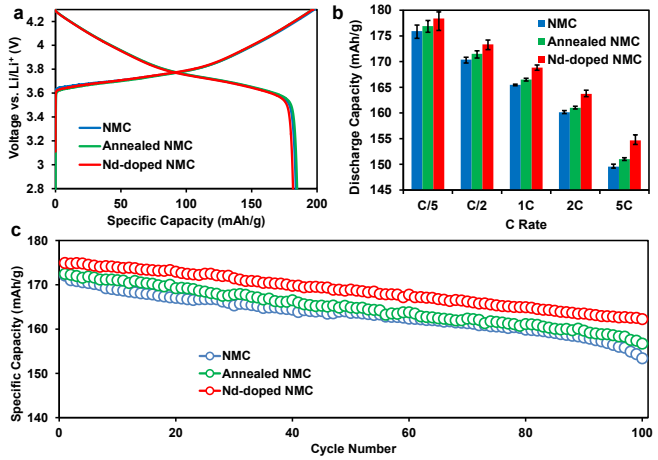

Fig. 3 (a) Typical voltage profiles of pristine and Nd-doped NMC in the first cycle at C/10 in coin cells. (b) Rate capability of pristine and Nd-doped NMC in coin cells, with error bars. (c) Specific discharge capacities of pristine and Nd-doped NMC at C/2 in coin cells.

The pristine NMC and Nd-doped NMC was further evaluated in single layer pouch (SLP) cells to confirm the enhanced cycling performance. During the first cycle at C/20, the Nd-doped NMC only shows a slight initial capacity drop compared to the pristine NMC. The capacity retention of the pristine and Nd-doped NMC powder is 74.1% and 87.1% after 300 cycles respectively, corresponding to specific discharge capacities of 118.2 and 138.3 mAh/g for the pristine and Nd-doped NMC, respectively (Fig. 4a). The Nd-doped NMC shows 17.5 % higher capacity retention than the pristine NMC after 300 cycles, which confirms that Nd doping significantly improves the cycling performance of NMC powder. In order to quantify the resistance growth over cycling, the direct current resistance (DCR) values based on a 10 s discharge pulse at 5C current (DCR=ΔV/I) were obtained every 50 cycles (Fig. 4b). Nd-doped NMC shows much slower DCR growth during cycling than the pristine NMC, specifically Nd-doped NMC has a resistance of 1.52 ohm after 300 cycles compared to 1.68 ohm for the pristine NMC. This slower resistance growth of Nd-doped NMC greatly contributes to its improved cycling performance.

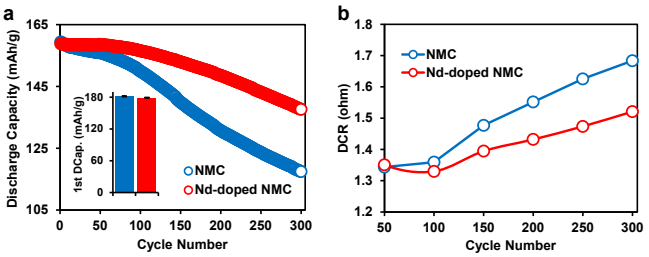

Fig. 4 (a) Specific discharge capacities of pristine and Nd-doped NMC at 1C in SLP cells. The inset shows the first discharge capacities at C/20, with error bars. (b) DCR values of pristine and Nd-doped NMC during cycling in SLP cells.

To better understand the role of Nd-doping on improving the cycling performance of NMC material, cross-sectional SEM images of the pristine and Nd-doped NMC after 300 cycles in SLP cells were obtained, as displayed in Fig. 5. The Nd-doped NMC shows far fewer cracks than the pristine NMC. Particles with more cracks will expose additional surface area, which increases the amount of side reactions and the formation of resistive layers.[20] Furthermore, the electrolyte may penetrate into the bulk through generated cracks.[21, 22] The formation and growth of cracks are closely related to the expansion and contraction of the crystal lattice during cycling. Therefore, *in-situ* XRD was performed during charging and discharging during the first cycle and after 100 cycles in coin cells (Fig. 6). The *a*, *c* lattice and volume of fresh (Fig. 6a-c) and cycled (Fig. 6d-f) NMC and Nd-doped NMC samples were plotted *vs.* voltage. The *a* lattice decreases during charging and increases during discharging (Fig. 6a), which is due to the smaller ionic radii of Ni^{3+} than Ni^{2+}.[23] The *c* lattice first increases during charging due to the electrostatic repulsion between the oxygen layers along *c* directions in a Li-deficient state,[24] then decreases upon further charging due to deep delithiation above 4 V (Fig. 6b).[25] The decrease of *c* lattice upon deep delithiation is reversible and *c* lattice increases again upon relithiation. The fresh Nd-doped NMC shows similar changes in lattice parameters with the non-doped NMC. After cycling, however, both samples show decreased *a*, *c* lattice and volume, indicating lattice collapse. The Nd-doped NMC shows less lattice collapse, reflected in its larger *a*, *c* lattice and volume. Such lattice collapse is one of the main reasons that lead to the formation and growth of cracks.[26] The lattice collapse may be caused by the phase change from layered to spinel/rock salt, accompanied by the oxygen loss, which happens on the surface and gradually extends to the bulk.[27] It is possible that the stronger Nd-O bond can suppress the oxygen loss, since the binding energy of Nd-O is 703 kJ/mol, which is significantly higher than that of Li-O (340.5 kJ/mol), Ni-O (366 kJ/mol), Co-O (397.4 kJ/mol), Mn-O (362 kJ/mol).[28] It is noted that the binding energy of Nd-O is also much higher than that of Al-O (501.9 kJ/mol), and Al is well known as a dopant that bonds with oxygen stronger than transition metals, therefore suppressing the O release.[6]

To understand how Nd doping affects the crystal structure on the surface of cycled electrodes, the cycled NMC and Nd-doped NMC samples ,after 300 cycles in SLP cells, were carefully examined by HR-TEM (Fig. 7). The NMC sample clearly shows rock salt phase near the surface region and

layered phase in the bulk region (Fig. 7a). The characteristic spots in FFT pattern of layered and rock salt phase can be indexed as $(012)_R$ and $(11\bar{1})_C$ (R for rhombohedral and C for cubic phase), respectively.[29] In comparison, the Nd-doped NMC only showed layered structure, attributed to (101) plane according to the d spacing (d=2.4456 Å). Nd surface doping greatly inhibited the surface phase change.

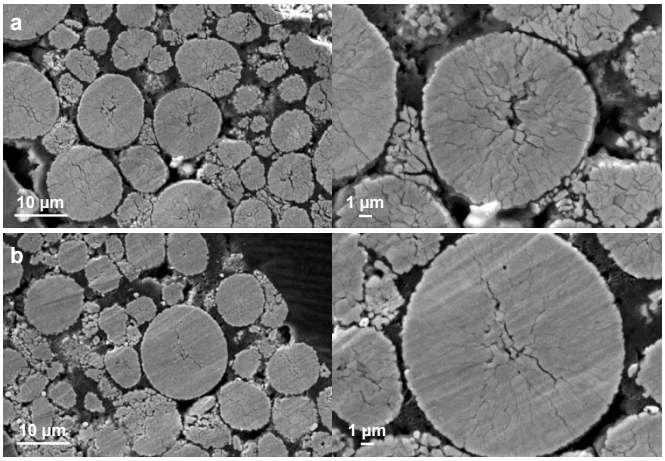

Fig. 5 Cross-section SEM images of (a) the pristine and (b) Nd-doped NMC after 300 cycles in SLP cells.

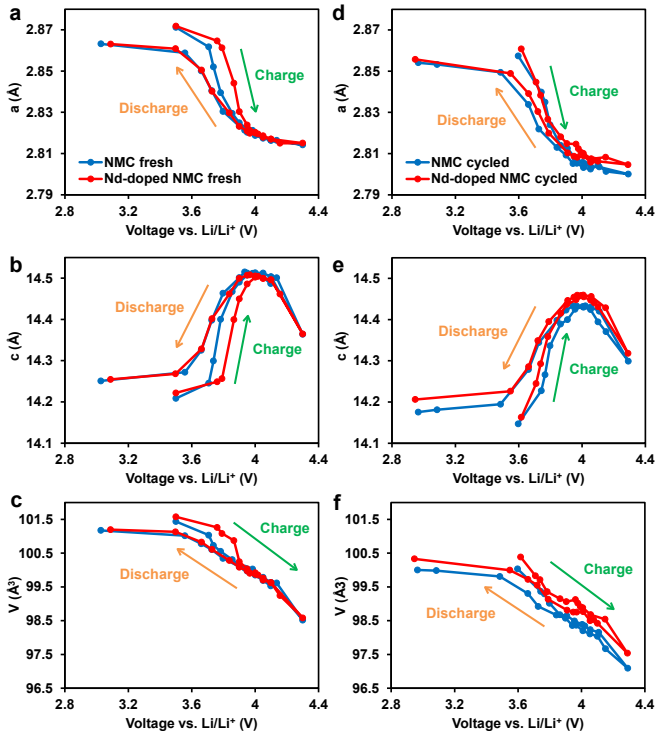

Fig. 6 Lattice parameters and volume evolution during charging and discharging via in-situ XRD. (a-c) Fresh NMC and Nd-doped NMC, (d-f) cycled NMC and Nd-doped NMC.

To examine the oxidation states of the transition metals on the surface and in the bulk, EELS linescans were performed on both fresh (before electrochemical testing) and cycled samples of NMC and Nd-doped NMC, with the lines in Fig. S4 indicating the positions of measurement. All the scans were obtained with constant spacing of 10 nm from the surface of the samples. Fresh NMC and Nd-doped NMC show similar EELS spectra (Fig. S5), however, after cycling their spectra are greatly different (Fig. 8). Fig. 8a and Fig. 8b show the O K-edge spectra of the cycled NMC and Nd-doped NMC samples, respectively. The broad peaks above 538 eV correspond to the transition of O 1s to the hybridized states, consisting of oxygen 2p and transition metal 4sp orbitals. The pre-edge peaks below 538 eV correspond to the transitions to the states of oxygen 2p and transition metal 3d orbitals.[30] The decreased pre-edge structure on the surface of cycled NMC (Fig. 8a) suggests the change of bond covalency between oxygen and transition metals, which is due to the formation of rock salt phase. In comparison, in the Nd-doped NMC there is not much difference of pre-edge structure from the bulk to the surface, which suggests stable surface structure. In Ni L-edge and Co L-edge spectra of the non-doped NMC (Fig. 8c and Fig. 8e), the peaks gradually shift to lower energies towards the surface, due to lower oxidation states of Ni (Ni^{2+}) and Co (Co^{2+}) on the surface, which further proves the existence of rock salt phases.[8] In contrast, in the Nd-doped NMC (Fig. 8d and Fig. 8f), the oxidation states of Ni and Co are almost identical from the bulk to the surface, suggesting greatly inhibited structural change by Nd surface doping. In Mn L-edge spectra of the non-doped NMC (Fig. 8g), the red shift of the peaks on the surface, corresponding to a lower oxidation state of Mn, is due to the surface oxygen loss during cycling, which is accompanied by the structural change from layered to spinel/rock salt phases.[31] The Nd-doped NMC (Fig. 8h) shows similar Mn L-edge peaks on the surface and in the bulk, which once again manifests the stabilized surface by Nd doping. The drastic difference in the EELS spectra of cycled NMC and Nd-doped NMC confirms the stabilized surface by Nd doping. As discussed earlier, the binding energy of Nd-O (703 kJ/mol) is much higher than Li-O (340.5 kJ/mol), Ni-O (366 kJ/mol), Co-O (397.4 kJ/mol), and Mn-O (362 kJ/mol), which helps suppress the oxygen loss and phase change.

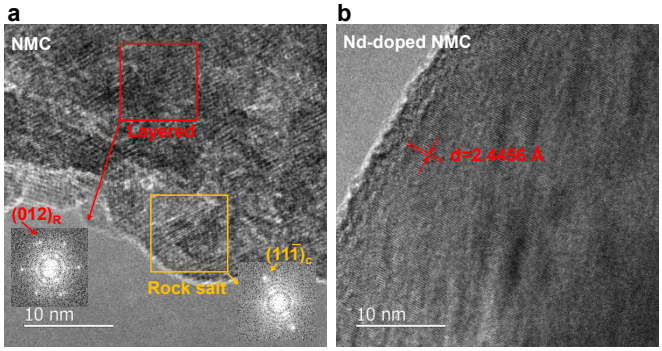

Fig. 7 HR-TEM images with selected FFT patterns of (a) NMC and (b) Nd-doped NMC cathodes after 300 cycles in SLP cells.

Nd doping significantly improves the cycling and rate performance of NMC cathode materials. In cross-sectional SEM and in-situ XRD measurement, the Nd-doped NMC sample shows far fewer cracks and less severe lattice collapse. In HR-TEM and EELS measurement, the Nd-doped NMC sample shows much less surface phase change. It is interesting that the surface doping technique has not only modified the surface, but also influenced the bulk properties, reflected in the internal cracks. The surface and bulk properties are closely correlated, since the phase change, accompanied by oxygen loss, may lead to lattice collapse which happens on the surface

and then gradually extends into the bulk. Surface stabilization itself can also help improve the cycling performance due to reduced formation of spinel/rock salt phases that are resistive to Li^+ diffusion. The two unique properties of Nd^{3+}, large ionic radius and high binding energy with oxygen, lead to the significantly enhanced rate and cycling performance of NMC cathode materials: the former can help expand the *c* lattice on the surface to improve the rate capability, and the latter can help suppress the surface phase change to improve the cycling capability.

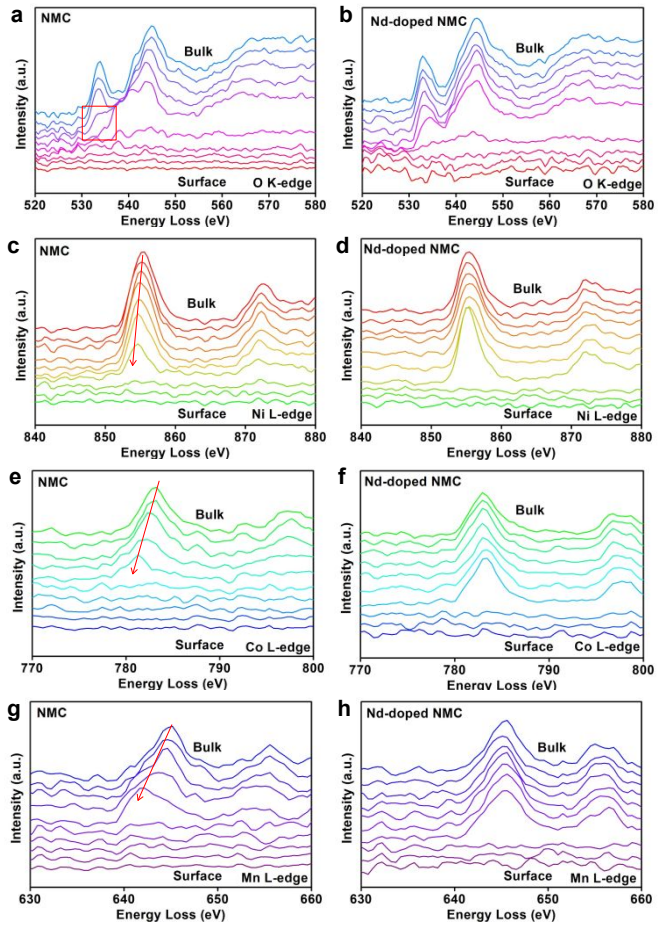

Fig. 8 EELS spectra of cycled NMC and Nd-doped NMC samples. (a-b) O K-edge, (c-d) Ni L-edge, (e-f) Co L-edge, and (g-h) Mn L-edge.

Dry surface doping has unique advantages over bulk doping and wet surface doping. Considering doping inevitably decreases the capacities of cathode materials, it is more efficient to limit the dopants on the surface to address the phase change issues since the surface is much less stable than the bulk. In addition, compared to the wet process, the dry process not only has low costs, but also raises no concern in leaching of Li caused by cathode-solvent contact. Critical parameters in dictating the surface doping depth/distribution include dopant, dopant content, uniformity of the mixture of doping agents and base materials, reaction temperature and time. Cathode materials with desired electrochemical properties may be acquired with different combinations of these parameters. Furthermore, this dry doping approach can be potentially used in green synthesis and modification of other cathode materials in lithium-ion or sodium-ion batteries.

Conclusions

In summary, a scalable surface dry doping technique with Nd_2O_3 as the doping agent, has been developed to improve the electrochemical performance of $LiNi_{0.64}Mn_{0.2}Co_{0.16}O_2$ cathode material. The cycling performance and rate capability of Nd-doped NMC have been significantly improved. It has been observed that Nd-doping can suppress the formation and growth of cracks during cycling, which is due to the suppressed lattice collapse, confirmed by in-situ XRD measurement of the fresh and cycled electrodes. HR-TEM images and EELS spectra show that the surface phase change is greatly suppressed by Nd surface doping. This surface doping technique shows great promise in improving the cycling performance of NMC cathodes. In addition, this work also sheds light on green synthetic strategies for energy storage materials.

Conflicts of interest

A provisional patent application 'Methods and Systems for Dry Surface Doping of Cathode Materials' was filed in May, 2019; US Provisional Application No. 62/845835. The non-provisional patent application was filed in May, 2020; Application NO. PCT/US20/30549.

Acknowledgements

Synchrotron diffraction measurements were performed at GeoSoilEnviroCARS (The University of Chicago, Sector 13), Advanced Photon Source (APS), Argonne National Laboratory. GeoSoilEnviroCARS is supported by the National Science Foundation – Earth Sciences (EAR – 1634415). This portion of the research used resources of the Advanced Photon Source, a U.S. Department of Energy (DOE) Office of Science User Facility operated for the DOE Office of Science by Argonne National Laboratory under Contract No. DE-AC02-06CH11357. Use of the Center for Nanoscale Materials, an Office of Science user facility, was supported by the U.S. Department of Energy, Office of Science, Office of Basic Energy Sciences, under Contract No. DE-AC02-06CH11357.

References

1 T. Placke, R. Kloepsch, S. Dühnen, M. Winter, *J. Solid State Electrochem.,* 2017, **21**, 1939-1964.
2 P. Meister, H. Jia, J. Li, R. Kloepsch, M. Winter, T. Placke, *Chem. Mater.,* 2016, **28**, 7203-7217.
3 Y. You, H. Celio, J. Li, A. Dolocan, A. Manthiram, *Angew. Chem. Int. Ed.,* 2018, **57**, 6480-6485.
4 U.-H. Kim, S.-T. Myung, C.S. Yoon, Y.-K. Sun, *ACS Energy Lett.,* 2017, **2**, 1848-1854.
5 Q. Liu, K. Du, H. Guo, Z.D. Peng, Y.B. Cao, G.R. Hu, *Electrochim. Acta,* 2013, **90**, 350-357.
6 S.W. Woo, S.T. Myung, H. Bang, D.W. Kim, Y.K. Sun, *Electrochim. Acta,* 2009, **54**, 3851-3856.
7 S. Liu, Z. Dang, D. Liu, C. Zhang, T. Huang, A. Yu, *J. Power Sources,* 2018, **396**, 288-296.
8 S.-K. Jung, H. Gwon, J. Hong, K.-Y. Park, D.-H. Seo, H. Kim, J. Hyun, W. Yang, K. Kang, *Adv. Energy Mater.,* 2014, **4**, 1300787.

9 H. Liu, H. Liu, I.D. Seymour, N. Chernova, K.M. Wiaderek, N.M. Trease, S. Hy, Y. Chen, K. An, M. Zhang, O.J. Borkiewicz, S.H. Lapidus, B. Qiu, Y. Xia, Z. Liu, P.J. Chupas, K.W. Chapman, M.S. Whittingham, C.P. Grey, Y.S. Meng, *J. Mater. Chem. A,* 2018, **6**, 4189-4198.
10 W. Cho, Y.J. Lim, S.-M. Lee, J.H. Kim, J.-H. Song, J.-S. Yu, Y.-J. Kim, M.-S. Park, ACS *Appl. Mater. Interfaces,* 2018, **10**, 38915-38921.
11 B. Han, B. Key, S.H. Lapidus, J.C. Garcia, H. Iddir, J.T. Vaughey, F. Dogan, *ACS Appl. Mater. Interfaces,* 2017, **9**, 41291-41302.
12 L. Zheng, T.D. Hatchard, M.N. Obrovac, *MRS Commun.,* 2018, **9**, 245-250.
13 P. Zhou, Z. Zhang, H. Meng, Y. Lu, J. Cao, F. Cheng, Z. Tao, J. Chen, *Nanoscale,* 2016, **8**, 19263-19269.
14 N. Machida, J. Kashiwagi, M. Naito, T. Shigematsu, *Solid State Ion.,* 2012, **225**, 354-358.
15 R. Shannon, *Acta Cryst. A,* 1976, **32**, 751-767.
16 C. Prescher, V.B. Prakapenka, *High Press. Res.,* 2015, **35**, 223-230.
17 B.H. Toby, R.B. Von Dreele, *J. Appl. Crystallogr.,* 2013, **46**, 544-549.
18 E.-S. Lee, A. Manthiram, *J. Mater. Chem. A,* 2013, **1**, 3118-3126.
19 J. Song, D.W. Shin, Y. Lu, C.D. Amos, A. Manthiram, J.B. Goodenough, *Chem. Mater.,* 2012, **24**, 3101-3109.
20 J. Xu, R.D. Deshpande, J. Pan, Y.-T. Cheng, V.S. Battaglia, *J. Electrochem. Soc.,* 2015, **162**, A2026-A2035.
21 H.-H. Sun, A. Manthiram, *Chem. Mater.,* 2017, **29**, 8486-8493.
22 P.-C. Tsai, B. Wen, M. Wolfman, M.-J. Choe, M.S. Pan, L. Su, K. Thornton, J. Cabana, Y.-M. Chiang, *Energy Environ. Sci.,* 2018, **11**, 860-871.
23 F. Wu, J. Tian, Y. Su, J. Wang, C. Zhang, L. Bao, T. He, J. Li, S. Chen, *ACS Appl. Mater. Interfaces,* 2015, **7**, 7702-7708.
24 D. Mohanty, S. Kalnaus, R.A. Meisner, K.J. Rhodes, J. Li, E.A. Payzant, D.L. Wood, C. Daniel, *J. Power Sources,* 2013, **229**, 239-248.
25 H. Li, P. Zhou, F. Liu, H. Li, F. Cheng, *J. Chen, Chem. Sci.,* 2019, **10**, 1374-1379.
26 J.-M. Lim, T. Hwang, D. Kim, M.-S. Park, K. Cho, M. Cho, *Sci. Rep.,* 2017, **7**, 39669.
27 F. Schipper, E.M. Erickson, C. Erk, J.-Y. Shin, F.F. Chesneau, D. Aurbach, *J. Electrochem. Soc.,* 2017, **164**, A6220-A6228.
28 Y. Luo, Taylor and Francis: Boca Raton, Florida, 2007.
29 Y. Shi, G. Chen, F. Liu, X. Yue, Z. Chen, *ACS Energy Lett.,* 2018, **3**, 1683-1692.
30 B. Qiu, M. Zhang, L. Wu, J. Wang, Y. Xia, D. Qian, H. Liu, S. Hy, Y. Chen, K. An, Y. Zhu, Z. Liu, Y.S. Meng, *Nat. Commun.,* 2016, **7**, 12108.
31 J. Graetz, C.C. Ahn, H. Ouyang, P. Rez, B. Fultz, *Phys. Rev. B,* 2004, **69**, 235103.

Table of Contents